

1  
2 **Frictional and Hydraulic Properties of Plate Interfaces Constrained by**  
3 **a Tidal Response Model Considering Dilatancy/Compaction**

4 **Ryunosuke Sakamoto<sup>1</sup> and Yoshiyuki Tanaka<sup>2</sup>**

5 <sup>1</sup>Department of Earth and Space Science, Osaka University, Osaka, Japan

6 <sup>2</sup>Department of Earth and Planetary Science, University of Tokyo, Tokyo, Japan

7 Corresponding author: Ryunosuke Sakamoto ([sakamoto@neq.ess.sci.osaka-u.ac.jp](mailto:sakamoto@neq.ess.sci.osaka-u.ac.jp))

8 **Key points:**

- 9
- The spring-slider model with dilatancy/compaction reproduces the observed tidal  
10 response of tremors during episodic tremor and slip (ETS).
  - The critical slip distance, diffusivity and effective stress are constrained by a comparison  
11 between the model and the observation.
  - The pore fluid pressure change due to dilatancy/compaction is dominant at the early stage  
12 of ETS, while it is negligible at the later stage.
- 13  
14  
15

## 16 **Abstract**

17 Tidal triggering of tectonic tremors has been observed at plate boundaries around the circum-Pacific region. It has  
18 been reported that the response of tremors to tidal stress during episodic tremor and slow slip (ETS) changes  
19 between the early and late stages of ETS. Several physical models have been constructed, with which observations  
20 for the tidal response during ETS have been partly reproduced. However, no model has been proposed that  
21 reproduces all the observations. In this study, a model adopted in previous studies is extended to include the effects  
22 of dilatancy/compaction that occur in the fault creep region. The analytical approximate solution derived in this  
23 study and numerical computational results reveal how the tidal response depends on physical properties of the fault.  
24 Furthermore, the model reproduces all the above observations simultaneously for a specific range of fault  
25 parameters. Of particular importance is that the occurrence of dilatancy/compaction is essential to reproduce the  
26 tidal response at the early stage of ETS. The value of the critical distance  $d_c$  is constrained to be approximately  
27 10 cm. This is in agreement with the values that have been widely used in seismic cycle numerical simulations  
28 rather than those obtained in laboratory experiments. The fluid pressure diffusivity is constrained to be at least  
29  $10^{-5}$  m<sup>2</sup>/s or less, and the effective normal stress is constrained to  $10^{5-6}$  Pa. In conclusion, this study shows that  
30 reproducing the tidal response of tectonic tremors during ETS is useful for estimating fault physical properties,  
31 including hydraulic properties.

## 32 **Plain Language Summary**

33 Slow earthquakes, which are slower fault slips than ordinary earthquakes, have been observed at many plate  
34 boundaries around the Pacific Rim. To understand how slow earthquakes occur, we need to know the exact physical  
35 fault properties that cause slow earthquakes. Previous studies have reported that the rate of occurrence of tectonic  
36 tremors, which are slow earthquakes, varies periodically in response to subsurface stress changes induced by tides.  
37 However, the detailed mechanism of the periodic behavior is still unclear. In this paper, we develop a theoretical  
38 model to explain this periodic behavior. A comparison between the observations in the Nankai Trough and Cascadia  
39 with our model shows that the pore fluid pressure in the vicinity of the fault changes significantly when tremors  
40 respond relatively weakly to tides. Furthermore, for the model to explain the observed tidal response of tremors, we  
41 find that the scale of the surface roughness of the fault should be much larger than those obtained by laboratory  
42 experiments and that the fault should have a low permeability.

## 43 **1 Introduction**

44 Recent geodetic and seismological observations have revealed that slow earthquakes occur in the transition zone,  
45 which is located at the deeper extension of the locked megathrust zone in a subduction zone. Slow earthquakes have  
46 various timescales, which are classified into low-frequency earthquakes (LFEs) with a major frequency of 2 – 8 Hz  
47 (Obara, 2002), tectonic tremors, which are aggregations of LFEs (Shelly et al., 2007a), very low-frequency  
48 earthquakes (VLFs) with a major frequency of 20 – 200 Hz (Ito et al., 2007), and slow slip events (SSEs), which  
49 do not radiate seismic waves and continue to slip for more than a few days (Dragert et al., 2001; Hirose et al., 1999).  
50 The focal mechanism of these slow earthquakes indicates that slow earthquakes accommodate shear slip on the plate  
51 interface (e.g., Ide et al., 2007; Shelly et al., 2006). This focal mechanism coincides with that of ordinary  
52 earthquakes, which cause fast slip. It is well known that the fast slip behavior of an ordinary earthquake reflects the  
53 physical properties of the fault, which consist of friction, effective normal stress and dilatancy/compaction (e.g.,  
54 Proctor et al., 2020; Scholz, 2019; Segall and Rice, 1995). The coincidence of the focal mechanism with those of  
55 slow earthquakes means that the slip behaviors of slow earthquakes should also reflect such fault physical  
56 properties. Therefore, it is important to clarify physical fault properties in the transition zone to reveal the  
57 mechanism of slow earthquakes on various timescales.

58 In numerical simulation studies, several models have been proposed to reproduce slow earthquakes. These models  
59 usually adopt the rate- and state-dependent friction law (RSF) (e.g., Dieterich, 1979; Marone, 1998) as the frictional  
60 law on the plate interface. Examples of such models are those assuming near-neutral stability (e.g., Liu and Rice,  
61 2005; Matsuzawa et al., 2010), dilatant strengthening of the shear zone (e.g., Liu, 2013; Segall et al., 2010),  
62 transition from velocity weakening (VW) at a low slip rate to velocity strengthening (VS) at a high slip rate (e.g., Im  
63 et al., 2020; Peng and Rubin, 2018; Shibazaki and Iio, 2003), spatial heterogeneity of frictional properties and  
64 effective normal stress (Luo and Ampuero, 2018), and sudden negative Coulomb stress change in the VS region due  
65 to fault valve action (Perfettini and Ampuero, 2008). Comparisons between such models and observed slow slip  
66 behaviors have allowed us to estimate the physical fault properties in the transition zone, which cannot be observed  
67 directly (e.g., Beeler et al., 2018; Luo and Liu, 2019; Nakata et al., 2012; Shibazaki et al., 2012).

68 In this study, we focus on tectonic tremors because they occur more frequently than other slow earthquakes, and it  
69 is easier to obtain more data to investigate the physical properties of faults. Tremors are classified into episodic  
70 families that accompany an SSE and continuous families that consist of tremors that occur almost every day

71 (Thomas et al., 2018). The former is called episodic tremor and slip (ETS) (Obara et al., 2004; Rogers and Dragert,  
 72 2003). An important observational fact is that, for an ETS, there is a correlation between the slip rate of the SSE and  
 73 the tremor occurrence rate (e.g., Bartlow et al., 2011; Hirose and Obara, 2010; Thomas et al., 2018; Villafuerte et al.,  
 74 2017), even though the cumulative moment magnitude  $M_w$  of tremors is orders of magnitude smaller than that of  
 75 SSEs (Kao et al., 2010). This correlation has been modeled by assuming that a tremor source is driven to failure by  
 76 the stress loading due to aseismic slip that occurs in the region surrounding the tremor source (Shelly et al., 2007a).  
 77 Based on this model, Shelly et al. (2011) interpreted the delayed dynamic triggering of tremors as a result of  
 78 transient creep induced by the passage of seismic waves. Similarly, Tan and Marsan (2020) interpreted that the  
 79 spatial anisotropy of the SSE during an ETS causes anisotropy in the power law describing a spatial decay of  
 80 tremors.

81 Another important observational fact revealed by global observations of tremors is that tremors are sensitive to  
 82 tidal stress (e.g., Chen et al., 2018; Hoston, 2015; Ide and Tanaka, 2014; Ide et al., 2015; Nakata, 2008; Royer et al.,  
 83 2015; Rubinstein et al., 2008; Shelly et al., 2007b; Thomas et al., 2009, 2012; Van Der Elst et al., 2016; Yabe et al.,  
 84 2015). In general, stress changes on faults in the transition zone due to semidiurnal and diurnal tides are a few kPa or  
 85 smaller. These stress changes are much smaller than the stress drop of ordinary earthquakes. Therefore, the tidal  
 86 response of ordinary earthquakes is not always noticeable (cf., Ide et al., 2016; Métivier et al., 2009; Vidale et al.,  
 87 1998). However, the tidal response of slow earthquakes is clearer because the pore pressure on the plate interfaces is  
 88 much higher in the transition zone than in the seismogenic zone, and hence, the effective normal stress is low (Audet  
 89 et al., 2009; Shelly et al., 2006).

90 The tidal response of tremors can be characterized by a tidal sensitivity and a phase difference. The tidal sensitivity,  
 91 which characterizes the magnitude of tidal modulation of the tremor rate (i.e., the number of observed tremor events  
 92 per unit time), is defined as  $\alpha$ ; the relationship between the tremor rate and the tidal Coulomb stress change is  
 93 described by

$$R = R_0 e^{\alpha \Delta S(t)}, \quad (1)$$

94 where  $R$  denotes the tremor rate,  $\Delta S(t)$  is the tidal Coulomb stress, and  $R_0$  is the reference tremor rate when  
 95  $\Delta S(t) = 0$ . In equation (1), the order of the tidal sensitivity is  $0.1 \sim 1 \text{ kPa}^{-1}$  (e.g., Houston, 2015; Ide et al., 2015;  
 96 Thomas et al., 2012; Yabe et al., 2015). The phase difference, defined as  $\delta$ , represents the phase shift between the  
 97 tremor rate peak (i.e., the phase at which  $R$  is maximized) and the tidal stress peak (i.e., the phase at which  $\Delta S(t)$  is

98 maximized).  $\delta$  is positive when the tremor rate reaches its maximum before the tidal stress reaches its maximum. For  
99 example, when the peak of  $R$  precedes the peak of  $\Delta S(t)$  in the semidiurnal tide (approximately 12 hour cycle) by 3  
100 hours,  $\delta \sim \pi/2$ . Previous studies have reported that  $\alpha$  and  $\delta$  change at the early and later stages of the ETS (Houston,  
101 2015; Royer et al., 2015; Yabe et al., 2015). At the early stage of an ETS,  $\alpha \sim 0.1 \text{ kPa}^{-1}$  (meaning that tidal  
102 modulation of the tremor rate is smaller) and  $\delta \sim \pi/2$ . At the later stage of the ETS,  $\alpha \sim 0.7 \text{ kPa}^{-1}$  (meaning that the  
103 tidal modulation of the tremor rate is larger) and  $\delta \sim 0$ . In addition, the number of tremors occurring at the later stage  
104 of ETS is approximately 1/10 or less than at the early stage of ETS (Houston, 2015; Royer et al., 2015).

105 Constructing a model that reproduces such observed tidal responses of tremors is an effective method to infer the  
106 physical properties of faults because tidal stress change, which serves as an “input” to a fault slip model to  
107 reproduce the tidal response, is much easier to estimate. Previous studies have proposed several models to interpret  
108 the observed tidal response of tremors (Ader et al., 2012; Beeler et al., 2013; Beeler et al., 2018; Hawthorne and  
109 Rubin, 2013; Houston, 2015). These models are classified into deterministic models that adopt the physical model  
110 proposed by Shelly et al. (2007a) and a stochastic model that adopts the Weibull distribution as the failure strength  
111 of tremor sources. Furthermore, deterministic models are classified into models that consider the change in the pore  
112 fluid pressure at the plate interface due to dilatancy/compaction and models that do not consider it (Table 1).

113 Specifically, Ader et al. (2012) adopted the RSF for the VS to describe the tidal modulation of the fault creep  
114 velocity. They showed that the tidal sensitivity and phase difference depend on the magnitude of the ratio of the  
115 timescale of a tidal period to the timescale of the evolution of the state variable. Based on this result, they stated that  
116 the differences in the tidal response of tremors are due to the differences in the average fault creep velocity. Beeler  
117 et al. (2013) compared dislocation creep, dislocation glide and the RSF of the VS as possible mechanisms of fault  
118 creep. They concluded that the RSF of the VS successfully explained the behavior represented by equation (1).

119 Based on a model that follows the RSF that transitions from the VW to the VS, Hawthorne and Rubin (2013)  
120 showed that the tidal modulation of the fault creep velocity increases as the fault creep average velocity decreases.

121 Based on a probabilistic model, Houston (2015) interpreted that the tidal response of tremors is different between  
122 the early stage and later stages of ETS due to a gradual decrease in the rupture strength for the tremor sources.

123 Beeler et al. (2018) reproduced the observed tidal response of tremors of the continuous families based on a model  
124 assuming the RSF of the VW and estimated fault physical properties of the transition zone, such as the fluid pressure  
125 diffusivity and dilatancy coefficient.

126

127 Table 1. A summary of previous models and our model

Paper that proposed the model	Model type	Introduction of fluid pressure change by dilatancy/compaction	Reproduction of tidal response of tremor at the early stage of ETS	Reproduction of tidal response of tremor at the later stage of ETS
Ader et al. (2012)	Deterministic	N	N	Y
Beeler et al. (2013)	Deterministic	N	N	Y
Hawthorne and Rubin (2013)	Deterministic	N	N	Y
Houston (2015)	Probabilistic	—	Y <sup>a</sup>	Y <sup>a</sup>
Beeler et al. (2018)	Deterministic	Y	— <sup>b</sup>	— <sup>b</sup>
This study	Deterministic	Y	Y	Y

128 <sup>a</sup> The model assumption may not be valid. <sup>b</sup>The model is not applicable to the tidal response of tremors during ETS.

129

130 Most of the above models can partially explain the observations of the tidal response of tremors during ETS (Table  
131 1). However, these models have several disadvantages. The model of Ader et al. (2012) cannot explain the  
132 observation results that  $\delta \sim \pi/2$  without adopting a value of a critical slip distance that is sufficiently smaller than  
133 that obtained from rock experiments. The models of Beeler et al. (2013) and Hawthorne and Rubin (2013) cannot  
134 explain the observation results of  $\delta \sim \pi/2$ . The model of Houston (2015) assumes that slip accumulation during the  
135 ETS breaks down precipitating minerals and weakens the fault. This model may contradict the idea of dilatant  
136 strengthening, which assumes that fault strength increases with increasing pore space due to breakage of  
137 precipitating minerals (Audet and Bürgmann, 2014). The model of Beeler et al. (2018) reproduces the tidal response  
138 of tremors for continuous families, but it cannot account for the tidal response of tremors during ETS. Therefore, the  
139 models proposed thus far cannot explain the aspects of the observed tidal responses of tremors or contradict the  
140 results of laboratory experiments.

141 Here, we propose a new model in which dilatancy/compaction occurs in the VS region to explain the observed tidal  
142 response of tremors during ETS. We find that the pore fluid pressure changes due to dilatancy/compaction caused by

143 tidal stress change in the transition zone, where the effective normal stress is low, has a significant influence on the  
 144 sliding behavior in the VS zone. We present governing equations for this problem in chapter 2. In the next chapter,  
 145 we derive an approximate solution to quantitatively describe  $\alpha$  and  $\delta$  and clarify how the model responds to tidal  
 146 stress changes. We reveal the physical reason for the dependence of  $\alpha$  and  $\delta$  on the fault physical properties. In  
 147 chapter 4, we estimate fault physical properties based on comparison between the observations and our model results  
 148 and discuss the validity of the estimated properties. In chapter 5, we summarize the results.

## 149 **2 Methods**

### 150 **2.1 Modeling the rate of tremor occurrence**

151 As in previous studies, we assume that tremors are generated by the rupture of small brittle patches on the fault  
 152 plane due to the aseismic shear slip of a larger-scale surrounding fault (Ader et al., 2012; Beeler et al., 2013; Shelly  
 153 et al., 2007a). This means that the tremor source is very small and that the tremor rate,  $R$ , serves as a passive meter  
 154 of the creep velocity of the surrounding fault,  $V$ :

$$\frac{V}{V_r} = \frac{R}{R_r}, \#(2)$$

155 where  $R_r$  and  $V_r$  denote the tremor rate and the creep velocity at a reference state, respectively. Based on this  
 156 assumption, we can regard a change in the tremor rate as a change in the creep velocity. We consider the effects of  
 157 tidal modulation on the creep velocity  $V$  rather than on the tremor rate itself (e.g., Ader et al., 2012; Beeler et al.,  
 158 2013; Ide and Tanaka, 2014).

### 159 **2.2 Governing equations**

#### 160 **2.2.1 RSF**

161 We model the above fault creep, assuming a one-degree-of-freedom spring-slider system and employ the RSF as a  
 162 friction law (Ader et al., 2012). According to the RSF, the friction coefficient  $\mu$  can be written as:

$$\mu = \mu_0 + a \log\left(\frac{V}{V_0}\right) + b \log\left(\frac{V_0 \theta}{d_c}\right), \#(3)$$

163 where  $\mu_0$  denotes the friction coefficient at a reference slip velocity  $V_0$ ,  $V$  is the slip velocity,  $d_c$  is the critical slip  
 164 distance,  $\theta$  is the state variable, which is often interpreted as the average contact time for an asperity, and  $a$  and  $b$   
 165 are fault constitutive parameters (e.g., Scholz, 1998). To represent fault creep, the constitutive parameters must  
 166 satisfy  $a > b$ . This regime is called VS. In equation (3), the second term on the right-hand side (RHS) represents the  
 167 “direct effect”, which is caused by a change in the slip velocity, and the third term on the RHS represents the  
 168 “evolution effect”, which is caused by the temporal change in the state variable. Fault slip behavior evolves to a new  
 169 steady state when a sudden slip velocity change occurs and the fault slips over a distance of  $d_c$  (Dieterich, 1979).  
 170 This process can be expressed in several ways. In this study, we adopt the slip law proposed by Ruina (1983):

$$\frac{d\theta}{dt} = -\frac{V\theta}{d_c} \log\left(\frac{V\theta}{d_c}\right). \#(4)$$

### 171 2.2.2 Dilatancy/Compaction

172 Dilatancy/compaction is a mechanism that relates fault gouge deformation to the behavior of the pore fluid. A  
 173 shear zone exists at and near the plate interface where shear slip is localized and fault gouge is present (e.g., Rice,  
 174 2006). We assume that the porosity change in the shear zone is caused by dilatancy/compaction (e.g., Segall et al.,  
 175 2010; Suzuki and Yamashita, 2009). The associated behavior of pore fluids can be modeled as in the following two  
 176 cases. The first is an undrained model, which assumes that the pore fluid pressure changes only within the shear  
 177 zone (Figure S1a in the supporting information), and the second is a drained model, which assumes a “homogeneous  
 178 diffusion” of the pore fluid into a region adjacent to the shear zone (Segall et al., 2010) (Figure S1b in the supporting  
 179 information). Since our model is a one-degree-of-freedom system, the pore fluid pressure is uniform in the direction  
 180 of the slip plane, and the pore fluid pressure diffuses in the direction vertical to the slip plane. As described later, the  
 181 undrained model can explain the observed results in a consistent way and the drained model cannot. Therefore, the  
 182 results for the drained model are shown only in the supporting information (Figures S3 and S4). The undrained  
 183 model is theoretically valid when a tidal period  $T$  (e.g., 12.4 hours) is sufficiently shorter than the characteristic  
 184 timescale  $t_w$  at which the pore fluid pressure diffuses through the shear zone ( $T \ll t_w$ ).

185 Mathematically, in the undrained model, the pore fluid pressure change in the shear zone can be described as

$$\frac{dp}{dt} = -M \frac{d\phi}{dt}, \#(5)$$

186 which is derived from the conservation of pore fluid mass (Segall et al., 1995), where  $dp/dt$  denotes a temporal  
 187 change in the pore fluid pressure,  $M$  is the bulk modulus of the fluid and the pore space, and  $d\phi/dt$  denotes a  
 188 change in the porosity due to dilatancy/compaction. As described previously, for the friction coefficient (equation  
 189 (3)), the porosity, which varies with dilatancy/compaction, also evolves from one steady state to another as the slip  
 190 velocity changes. The evolution law for the porosity can be empirically described as

$$\frac{d\phi}{dt} = -\frac{\epsilon}{\theta} \frac{d\theta}{dt}, \#(6)$$

191 using the state variable  $\theta$ , where  $\epsilon$  is a dilatancy coefficient (Segall and Rice, 1995). From equations (5) and (6), we  
 192 obtain

$$\frac{dp}{dt} = -\epsilon M \frac{1}{\theta} \frac{d\theta}{dt}. \#(7)$$

193

### 194 2.2.3 A quasi-static equation of motion

195 The quasi-static equation of motion for the one-degree-of-freedom spring-slider model under tidal stress can be  
 196 written as

$$\Delta\tau(t) + k\Delta u = \mu\sigma_{eff}(t), \#(8)$$

197 where  $\Delta\tau(t)$  denotes the shear stress acting on the fault plane due to tides,  $\sigma_{eff}(t)$  is the effective normal stress,  $\Delta u$   
 198 is the relative displacement of the block to the spring pulling distance,  $k$  is the spring stiffness and  $\mu$  is the friction  
 199 coefficient (Ader et al., 2012; Perfettini and Schmittbuhl, 2001). In our model, the effective normal stress is written  
 200 as  $\sigma_{eff}(t) = \sigma_{eff}^0 + \Delta\sigma(t) - \Delta p(t) - \Delta p'(t)$ , where  $\sigma_{eff}^0$  denotes a reference effective normal stress,  $\Delta\sigma(t)$  is the  
 201 normal stress acting on the fault plane due to tides,  $\Delta p(t)$  is the pore fluid pressure change due to  
 202 dilatancy/compaction in the shear zone, and  $\Delta p'(t)$  is the pore fluid pressure change due to the tidal normal stress  
 203 change. When the tidal normal stress increases,  $\Delta p'(t)$  also increases in proportion to the Skempton coefficient,  $B$   
 204 (i.e.,  $\Delta p'(t) = B\Delta\sigma(t)$ ) (e.g., Beeler et al., 2018; Scholz et al., 2019). Using this relationship, the effective normal  
 205 stress can be rewritten as

$$\sigma_{eff}(t) = \sigma_{eff}^0 + (1 - B)\Delta\sigma(t) - \Delta p(t). \#(9)$$

206 The observations show that there is almost no correlation between the tidal normal stress change and the tremor  
 207 rate (Houston, 2015; Thomas et al., 2012), which indicates that the fault strength is almost unchanged due to the

208 tidal normal stress change. This suggests that  $B$  is nearly equal to 1 (equation (9)). Therefore, we adopt  $B = 0.9$  in  
 209 our model. For simplicity, we assume that the tidal stresses  $\Delta\sigma(t)$  and  $\Delta\tau(t)$  have a single period with the same  
 210 magnitude and phase (i.e.,  $\Delta\sigma(t) = \Delta\tau(t) = |\Delta\sigma(t)|e^{i\omega t}$ ).

211

### 212 2.3 Nondimensionalization of governing equations

213 Equations (3), (4), (7) and (8) constitute the governing equations for our model. For nondimensionalization of these  
 214 equations, we selected a tidal period  $T$ , a reference effective normal stress  $\sigma_{eff}^0$ , and a critical slip distance  $d_c$  as  
 215 characteristic physical quantities (Table 2). Representing the dimensionless variables with a tilde, the result is  
 216 written as:

$$\mu = \mu_0 + a \log\left(\frac{\tilde{V}}{\tilde{V}_0}\right) + b \log\left(\frac{\tilde{\theta}}{\tilde{\theta}_0}\right)$$

$$\Delta\tilde{\tau} + \tilde{K}\Delta\tilde{u} = \mu\tilde{\sigma}_{eff}$$

$$\frac{d\tilde{\theta}}{d\tilde{t}} = -\tilde{\theta}\tilde{V}\log(\tilde{\theta}\tilde{V})$$

$$\frac{d\tilde{p}}{d\tilde{t}} = \frac{U}{\tilde{\theta}} \frac{d\tilde{\theta}}{d\tilde{t}}, \#(10)$$

217 where  $\theta_0 = d_c/V_0$  denotes the state variable at a reference slip velocity  $V_0$ ,  $\tilde{K} = d_c k/\sigma_{eff}^0$  is the nondimensional  
 218 spring constant, and  $U = M\epsilon/\sigma_{eff}^0$  is the dilatancy parameter. Substituting the last equation in equation (10) into the  
 219 nondimensionalized version of equation (9), we find that the larger  $U$  is, the more dominant the effect of  $\Delta p(t)$  on  
 220 the effective normal stress is. In other words, the parameter  $U$  represents the relative importance of the  
 221 dilatancy/compaction to the effective normal stress change. Previous experiments and observations suggest that  
 222  $\sigma_{eff}^0 \sim 10^{5\sim 6}$  Pa (Nakata et al., 2008; Shelly et al., 2006; Yabe et al., 2015),  $\epsilon \sim 10^{-4\sim -5}$  (Samuelson et al., 2009),  
 223 and  $M \sim 10^{10}$  Pa (Segall et al., 1995). This yields a possible range of  $U$  from  $10^0$  to  $10^{-2}$ .

224 The time evolution of each physical quantity is numerically calculated using the third-order Adams-Bashforth  
 225 method.

226

227 Table 2. Parameters of fault physical properties

Parameter	Value
Reference velocity $V_0$	$10^{-9}$ m/s
Spring pulling velocity $V_{pl}$	$10^{-8}$ m/s
Reference frictional coefficient $\mu_0$	0.7
Reference effective normal stress $\sigma_{eff}^0$	500 kPa
Skempton coefficient $B$	0.9
Spring stiffness $k$	$10^4$ Pa/m
Magnitude of tidal shear stress $ \Delta\tau(t) $	1 kPa
Magnitude of tidal normal stress $ \Delta\sigma(t) $	1 kPa
Tidal period $T$	12.4 h
Frictional parameter $a$	0.003
Frictional parameter $b$	0.002
Dilatancy parameter $U$	$10^{-2-0}$

228

229 

#### 2.4 Definition of the tidal sensitivity ( $\alpha$ ) and the phase difference ( $\delta$ )

230 In previous studies,  $\alpha$  has been estimated using equation (1), and  $\delta$  has been inferred using the phase difference  
231 between the tidal Coulomb stress peak and the tremor rate peak (Houston, 2015; Royer et al., 2015; Yabe et al.,  
232 2015); we define  $\alpha$  and  $\delta$  in the same way. In the following, we refer to these two parameters as the “tidal  
233 response”.

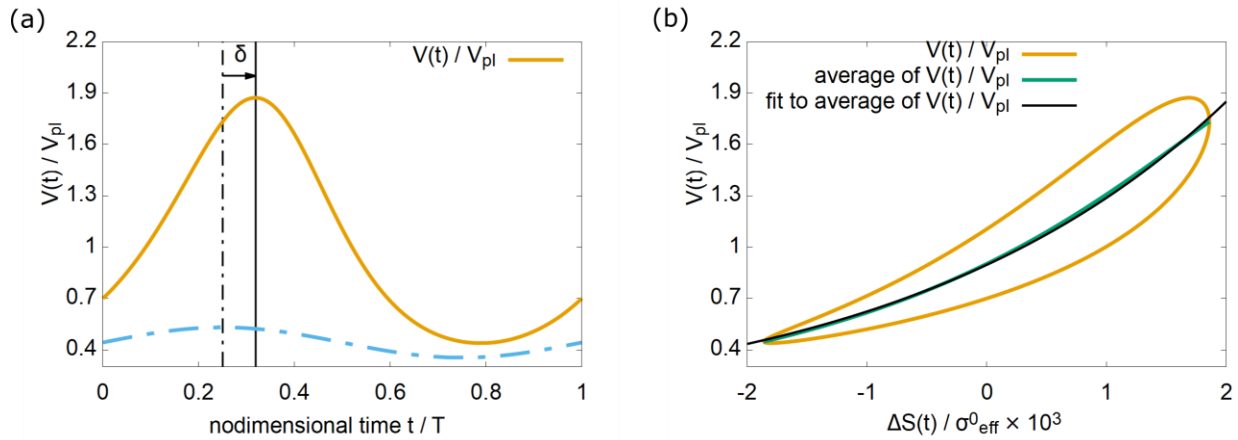
234 To illustrate the definition of these two quantities and how to determine them, Figure 1 shows a result obtained by  
235 numerically solving the governing equations for the case of  $U = 0$  and  $d_c = 100$   $\mu\text{m}$ . The solid yellow line in  
236 Figure 1a is the time evolution of  $V(t)/V_{pl}$  during one tidal cycle. The solid yellow line in Figure 1b shows  $V(t)/$   
237  $V_{pl}$  in Figure 1a against  $\Delta S(t)$ , and the solid green line shows the average of the upper and the lower values of  
238  $V(t)/V_{pl}$  at each  $\Delta S(t)$  on the horizontal axis, where

$$\Delta S(t) = \Delta\tau(t) - \mu_{pl}(1 - B)\Delta\sigma(t) \#(11)$$

239 denotes the tidal Coulomb stress (e.g., Beeler et al., 2018; Scholz et al., 2019), and  $\mu_{pl}$  is the steady-state friction  
 240 coefficient at velocity  $V_{pl}$ . The reason why  $\Delta S(t)$  is described by  $\Delta\tau(t) - \mu_{pl}(1 - B)\Delta\sigma(t)$  instead of  $\Delta\tau(t) -$   
 241  $\mu_{pl}\Delta\sigma(t)$  is that, for a poroelastic medium, the effective normal stress change due to tides is described by  $(1 -$   
 242  $B)\Delta\sigma(t)$  from equation (9).  $\alpha$  is obtained by fitting the following equation to the average of  $V(t)/V_{pl}$  (solid green  
 243 line in Figure 1b):

$$\frac{V(t)}{V_{pl}} = ce^{\alpha\Delta S(t)}. \#(12)$$

244 In the fitting, a constant  $c(< 1)$  is simultaneously determined. The time average of  $e^{\alpha\Delta S(t)}$  for one tidal cycle is  
 245 greater than 1 when  $\alpha$  is sufficiently large. Therefore, if  $c$  is not introduced, the time average of  $V(t)$  over one tidal  
 246 cycle exceeds  $V_{pl}$ . This implies that forward slip accumulates in the long run, which is seismologically unrealistic. A  
 247 similar constant is used in Beeler et al. (2018). The value of  $c$  is presented in Figure S2 in the supporting  
 248 information. The solid black line in Figure 1b shows the fitted result.  $\delta$  is defined as the phase difference between  
 249 the  $\Delta S(t)$  peak and the  $V(t)/V_{pl}$  peak (see  $\delta$  of Figure 1a), where  $\delta$  is positive when the  $V(t)/V_{pl}$  peak precedes the  
 250  $\Delta S(t)$  peak (i.e.,  $\delta$  in Figure 1a is negative).  
 251



252  
 253 Figure 1. The numerical solution of equation (10) for  $U = 0$  and  $d_c = 100 \mu\text{m}$ . (a) Determination of the phase  
 254 difference ( $\delta$ ). The horizontal axis denotes time normalized by the tidal cycle, and the value from 0 to 1 indicates  
 255 one tidal cycle. The vertical axis represents the slip velocity normalized by the reference velocity,  $V(t)/V_{pl}$ . The  
 256 solid yellow line shows  $V(t)/V_{pl}$ , and the dashed blue line shows the tidal Coulomb stress,  $\Delta S(t)$ . The dashed black  
 257 line represents the phase when  $\Delta S(t)$  reaches the maximum, and the solid black line represents the  $V(t)/V_{pl}$  peak.

258 The phase difference  $\delta$  is defined so that it is positive when the  $V(t)/V_{pl}$  peak precedes the  $\Delta S(t)$  peak. (b)  
 259 Determination of the tidal sensitivity ( $\alpha$ ). The horizontal axis is  $\Delta S(t)$  normalized by  $\sigma_{eff}^0$ . The vertical axis  
 260 represents the slip velocity normalized by the reference velocity,  $V(t)/V_{pl}$ . The solid yellow line shows  $V(t)/V_{pl}$  in  
 261 (a). The solid green line shows the average of the upper and lower velocities at each value of  $\Delta S(t)$ .  $c$  and  $\alpha$  in  
 262 equation (12) are determined by a least squares method by fitting equation (12) against the green solid line. The  
 263 solid black line shows the fitted result.

## 264 2.5 An approximate solution for $\alpha$ and $\delta$

265 To clarify how the tidal responses depend on the fault physical properties, we analytically derived an approximate  
 266 solution for  $\alpha$  and  $\delta$ . The result is shown in Section 3.1.

## 267 3 Result

### 268 3.1 Derivation and verification of the approximate solution

269 When the magnitude of the tidal Coulomb stress change  $|\Delta S(t)|$  is small enough ( $|\Delta S(t)| \ll (a - b)\sigma_{eff}^0$ ), we can  
 270 assume that the perturbation of each physical quantity caused by  $|\Delta S(t)|e^{i\omega t}$  is proportional to  $e^{i\omega t}$ , where  $\omega =$   
 271  $2\pi/T$  is the angular velocity of the tide (Segall, 2010; Ader et al., 2012). In other words, the physical quantities can  
 272 be written as  $V(t) = V_{pl} + \Delta V e^{i\omega t}$ ,  $\theta(t) = \theta_{pl} + \Delta\theta e^{i\omega t}$  and  $p(t) = p_0 + \Delta p e^{i\omega t}$ , where  $\theta_{pl}$  denotes the steady-  
 273 state variable at  $V = V_{pl}$ ,  $p_0$  is the reference value of pore fluid pressure, and  $\Delta V$ ,  $\Delta\theta$  and  $\Delta p$  are the magnitudes of  
 274 the perturbation. Substituting these forms into equations (3), (4), (7), and (8), and after some algebra, the  
 275 perturbation of the nondimensionalized slip velocity,  $\Delta\tilde{V}$ , can be written as

$$\frac{\Delta\tilde{V}}{\tilde{V}_{pl}} = \frac{2\pi i}{\tilde{K}\tilde{V}_{pl} + 2\pi i A} |\Delta\tilde{S}(t)|, \#(13)$$

276 where

$$A = a - \frac{1}{1 + i\frac{T_\theta}{T}} (b - \mu_{pl}U) \#(14)$$

277 and

$$T_\theta = 2\pi \frac{d_c}{V_{pl}}. \#(15)$$

278 Equation (15) represents a characteristic timescale on which the state variable evolves (Ader et al., 2012). From the  
 279 relationship of  $\Delta\tilde{V}e^{i\omega t} = \tilde{V}(t) - \tilde{V}_{pl}$ , equation (13) can be rewritten as  $V(t)/\tilde{V}_{pl} = 1 + 2\pi i\Delta\tilde{S}(t)/(\tilde{K}\tilde{V}_{pl} + 2\pi iA)$ .  
 280 We assume that this equation is the Taylor expansion of the RHS of

$$\frac{\tilde{V}(t)}{\tilde{V}_{pl}} = \exp\left(\frac{2\pi i}{\tilde{K}\tilde{V}_{pl} + 2\pi iA}\Delta\tilde{S}(t)\right) \#(16)$$

281 to the first order. Then, comparing equation (16) with equation (1), we find that the tidal sensitivity ( $\alpha$ ) and the  
 282 phase difference ( $\delta$ ) can be written as

$$\alpha = \text{Re}\left(\frac{2\pi i}{(\tilde{K}\tilde{V}_{pl} + 2\pi iA)\sigma_{eff}^0}\right) \#(17)$$

$$\delta = \text{arg}\left(\frac{2\pi i}{\tilde{K}\tilde{V}_{pl} + 2\pi iA}\right) \#(18)$$

283 For  $U = 0$ , where dilatancy/compaction is neglected, Ader et al. (2012) presented a linearized approximation  
 284 solution and a numerical solution. We can confirm that equations (13) and (18) are consistent with the  
 285 nondimensionalized version of equation (3) of Ader et al. (2012), who examined tidal responses for different values  
 286 of  $T$ . However, how the tidal response changes with different values of  $d_c$  was not studied in detail for the period of  
 287  $\sim 12$  h, which is the dominant period of tides. Therefore, we examined how the tidal response changes with changes  
 288 in  $d_c$  or  $T_\theta$  (equation (15)) for this period, since a comparison between our model and observations of the tidal  
 289 response enables us to infer  $d_c$  in the actual geophysical situation. Figures 2a and 2b show  $\alpha$  and  $\delta$ , respectively. In  
 290 these figures, the solid green line and green dots represent the numerical solution of equation (10) and the  
 291 approximate solution, respectively. The approximate solution and the numerical solution agree with each other  
 292 within 15% for most cases. When  $T_\theta/T \sim 10^{-1}$ , the approximate solution is less accurate for both  $\alpha$  and  $\delta$ . This  
 293 means that the accuracy of the approximate solution can deteriorate when the nonlinearity is stronger (i.e.,  $\alpha$  is  
 294 larger).

295 For  $U \neq 0$ , the approximate solution agrees with the numerical solution within 15% in all cases. The good  
 296 agreement is attributed to the fact that  $\alpha$  is relatively small (at most  $\sim 0.7$  kPa $^{-1}$ ), thus the nonlinearity is weaker.  
 297 This indicates that the approximate solution is valid regardless of the value of  $T_\theta/T$  when  $U \neq 0$ .

## 3.2 Dependence of the tidal response on the fault physical properties

Based on the approximate solution and an analysis of the quasi-static equation of motion, we clarify how  $\alpha$  and  $\delta$  during an ETS depend on the fault physical properties. The specific range of physical properties that can explain the observations is discussed in Section 4.

### 3.2.1 Factors governing the tidal response during ETS

In our model,  $V_{pl}$  represents the average creep velocity of the surrounding fault. We can apply this model to fault creep during ETS, which occurs over a shorter time span than secular plate subduction. Geodetic observations show that the fault creep velocity during an ETS is  $\sim 10^{-6\sim-8}$  m/s (e.g., Meade and Loveless, 2009; Schwartz and Rokosky, 2007). Therefore, we set  $V_{pl}$  as  $10^{-8}$  m/s in the following numerical simulation. In addition, the frictional parameters  $a$  and  $b$  are chosen so that  $a - b$  is small because it has been suggested that  $a - b$  decreases in the transition zone (e.g., Liu, 2013; Matsuzawa et al., 2010). The other parameters are similar to those used in previous studies (Ader et al., 2012; Hawthorne and Rubin, 2013). Table 2 shows the adopted parameters. For these parameters, we can confirm that  $|\tilde{K}\tilde{V}_{pl}| \ll |2\pi iA|$ . Then, the tidal response (equations (17) and (18)) can be approximated as

$$\alpha \sim \text{Re}\{(A\sigma_{eff}^0)^{-1}\} \quad \#(19)$$

$$\delta \sim \text{arg}\{A^{-1}\}. \quad \#(20)$$

Combining these equations with equation (14), we note that  $\alpha$  and  $\delta$  depend on  $T_\theta/T$  and  $U$ . The former parameter  $T_\theta/T$  prescribes whether there is enough time for the state variable to evolve throughout a tidal cycle. For example,  $T_\theta/T \ll 1$  means that there is enough time for the state variable to evolve throughout a tidal cycle. In the following, we focus on these two parameters,  $T_\theta/T$  and  $U$ , to discuss the tidal response.

### 3.2.2 A balance of the stress changes

From Figures 2a and 2b, we see a large difference between the cases for  $U = 0$  and  $U \neq 0$ . The reason for this large difference can be understood by using the following equation, which is derived from the quasi-static equation of motion (equation (8)) (for the derivation, see Appendix A):

$$\Delta S(t) \sim \sigma_{eff}^0 \left( -\mu_{pl} U \ln \left( \frac{\theta}{\theta_{pl}} \right) + a \ln \left( \frac{V}{V_{pl}} \right) + b \ln \left( \frac{\theta}{\theta_{pl}} \right) \right). \#(21)$$

320 In equation (21), the left-hand side (LHS) and the RHS correspond to the tidal Coulomb stress and the frictional  
 321 strength, respectively. The first, second, and third terms on the RHS represent the dilatancy/compaction effect, the  
 322 direct effect, and the evolution effect, respectively. In equation (21),  $U$  is included only in the first term (the  
 323 dilatancy/compaction term) on the RHS. When  $U = 0$ , the first term vanishes and the tidal response (equations (19)  
 324 and (20)) obtained in this study is consistent with the result discussed in Chapter 4.1 of Hawthorne and Rubin  
 325 (2013). Therefore, we analyze the tidal response for  $U \neq 0$  below.

### 326 3.2.3 Analysis of the tidal response for $U \neq 0$

327 Figures 2a and 2b show that the tidal response can be classified into three cases according to the value of  $T_\theta/T$   
 328 because the value affects the degree to which the first term of  $a\{1 - (b - \mu_{pl}U)/a(1 + iT_\theta/T)\}$  is dominant (see  
 329 Equation (14)). The condition for the first term on the RHS of equation (14) to be negligibly small is  $|b -$   
 330  $\mu_{pl}U|/a|1 + iT_\theta/T| \ll 1$ . Using the parameter set shown in Table 2, we obtain  $|b - \mu_{pl}U|/a \sim O(1)$ , so  $T_\theta/T \gg$   
 331  $|b - \mu_{pl}U|/a$  is required for the above inequality to hold. Conversely, the condition for the first term on the RHS of  
 332 equation (14) becoming dominant is when the value of  $a(1 + iT_\theta/T)$  becomes  $\sim a$ . In other words,  $T_\theta/T \ll 1$ . The  
 333 other case is the intermediate region between these two limits.

334 First, we consider the case where  $T_\theta/T \gg |b - \mu_{pl}U|/a$ . We find that for larger values of  $T_\theta/T$ ,  $\alpha$  and  $\delta$  converge  
 335 to the same values regardless of the value of  $U$  ( $T_\theta/T \sim 10^4$  in Figures 2a and 2b). When  $T_\theta/T \gg |b - \mu_{pl}U|/a$ , the  
 336 first term on the RHS of Equation (14) can be ignored ( $A \sim a$ ). Therefore, substituting  $A \sim a$  into Equations (19) and  
 337 (20),  $\alpha$  and  $\delta$  become  $a\sigma_{eff}^0$  and 0, respectively, regardless of the value of  $U$ . Because there is not enough time for  
 338 the state variable to evolve, the state variable is almost constant ( $\theta \sim \theta_{pl}$ ). Then, the dilatancy/compaction and the  
 339 evolution effect term of equation (21) are almost zero. Therefore, equation (21) can be approximated as

340  $\Delta S(t) \sim a\sigma_{eff}^0 \log(V/V_{pl})$  or  $V \sim V_{pl} e^{\Delta S(t)/a\sigma_{eff}^0}$ . This means that  $\alpha = 1/a\sigma_{eff}^0$ . Moreover, the form of this equation  
 341 indicates that the slip velocity peak agrees with the tidal Coulomb stress peak in time, which means that  $\delta = 0$ .

342 Next, we consider the case where  $T_\theta/T \ll 1$ . In this case,  $\alpha$  depends on  $U$  and takes a small value when  $U$  is large  
 343 ( $T_\theta/T \sim 10^{-2}$  in Figure 2a). However,  $\delta$  converges to zero regardless of the value of  $U$  ( $T_\theta/T \sim 10^{-2}$  in Figure 2b).

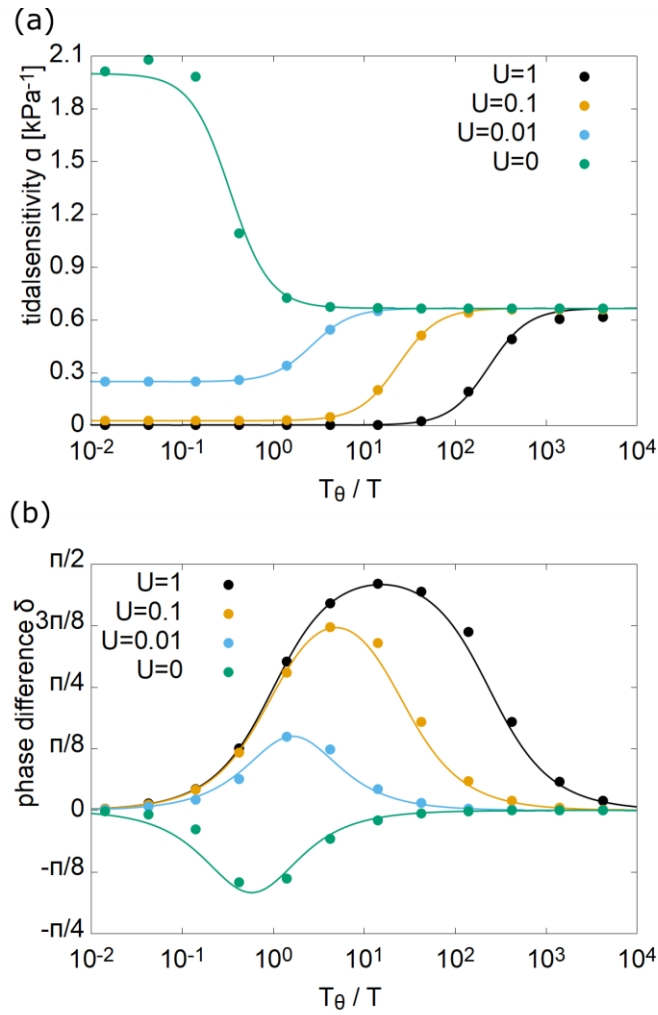
344 When  $T_\theta/T \ll 1$ , we obtain  $\alpha = 1/(a - b + \mu_0 U)\sigma_{eff}^0$  and  $\delta = 0$  from equations (14), (19) and (20). Because the  
 345 state variable evolves more rapidly than the tidal Coulomb stress change, the state variable is close to the new  
 346 steady-state value ( $\theta \sim d_c/V$ ). This is derived by considering  $d\theta/dt \sim 0$  in equation (4). Then, equation (21) can be  
 347 approximated as  $\Delta S(t) \sim (a - b + \mu_{pl} U)\sigma_{eff}^0 \log(V/V_{pl})$ . As before, the form of this equation explains the above  
 348 values of  $\alpha$  and  $\delta$ . Moreover, it is clear from the form of  $\alpha$  that it decreases as  $U$  increases.

349 Finally, we consider the case of the intermediate region between the above two limits. Figure 2a shows that  $\alpha$  varies  
 350 smoothly and connects the limit values for  $T_\theta/T \gg |b - \mu_{pl} U|/a$  and  $T_\theta/T \ll 1$  ( $T_\theta/T \sim 10^{0 \sim 1}$  in Figure 2a). Figure  
 351 2b shows that the maximum value of  $\delta$  approaches  $\pi/2$  as  $U$  increases ( $T_\theta/T \sim 10^{0 \sim 1}$  in Figure 2b). To clarify why  
 352 this occurs, we compared the time variation of the tidal Coulomb stress term ( $\Delta S(t)$  of equation (21)), the  
 353 dilatancy/compaction effect term and the evolution effect term in equation (19). Figure 3 shows these three terms for  
 354  $U = 1$  and  $U = 0.01$ . For  $U = 1$ , the dotted blue line representing the tidal Coulomb stress and the solid black line  
 355 representing the dilatancy/compaction effect are almost identical except for a small phase difference. Representing  
 356 this phase difference as  $\beta (\ll \pi)$ , we see from the balance between the solid black line and the dot blue line in Figure  
 357 3 that  $-\mu_{pl} U \sigma_{eff}^0 \log(\theta/\theta_{pl}) \sim |\Delta S(t)| e^{i\omega(t-\beta)}$ . The dashed black line representing the evolution effect is negligibly  
 358 small ( $b \sigma_{eff}^0 \log(\theta/\theta_{pl}) \sim 0$ ). Substituting these into equation (21), and after some algebra (Appendix B), we find  
 359 that

$$\log\left(\frac{V}{V_{pl}}\right) \propto \text{Re}\left\{e^{i\omega\left(t+\frac{\pi}{2}\right)}\right\}. \#(22)$$

360 This indicates that the slip velocity peak agrees with the tidal Coulomb stress rate peak ( $T_\theta/T \sim 10^1$  in Figure 2a).  
 361 For  $U = 0.01$ , the phase difference  $\delta$  is small. This can be explained by considering the balance in equation (21).  
 362 The amplitude of the solid yellow line representing the dilatancy/compaction effect in equation (21) is smaller than  
 363 the amplitude of the dotted blue line representing the tidal Coulomb stress. Furthermore, the dashed yellow line  
 364 representing the evolution effect decreases when the dilatancy/compaction effect term (solid yellow line) is larger  
 365 and vice versa. Therefore, the amplitude of the sum of these two effects becomes even smaller than the amplitude of  
 366  $\Delta S(t)$ . For the stress balance of equation (21) to be satisfied, the direct effect term (second term on the RHS) should  
 367 balance the difference between  $\Delta S(t)$  and the sum of the above two effects. This means that the smaller  $U$  becomes,  
 368 the larger the direct effect term. The dominance of the direct effect term indicates that  $\delta$  is small, as we have seen  
 369 for the case of  $T_\theta/T \gg |b - \mu_{pl} U|/a$ , which explains why  $\delta$  is closer to zero for  $U = 0.01$  than for  $U = 1$ .

370



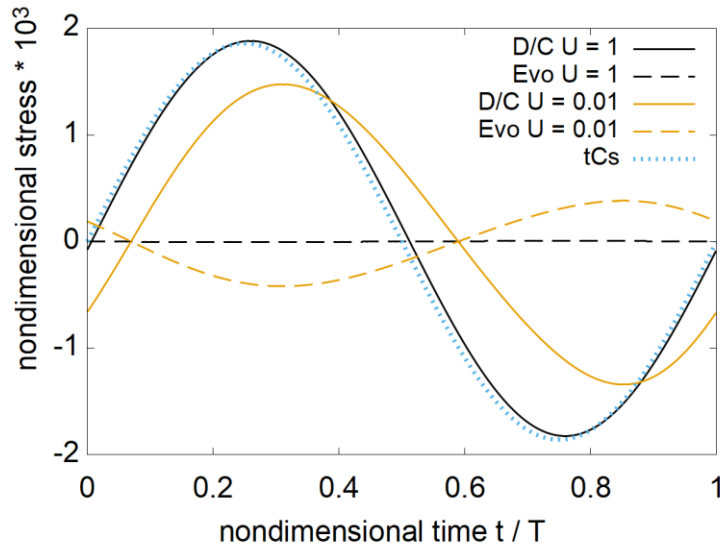
371

372 Figure 2. (a) The numerical solution of  $\alpha$  (dots) and the approximation solution (equation (19)) (solid line). (b) The

373 numerical solution of  $\delta$  (dots) and the approximation solution (equation (20)) (solid line). The differences in color

374 represent the differences in the dilatancy parameter  $U$ .

375



376

377 Figure 3. Time evolution of the tidal Coulomb stress (tCs) (blue dotted line), the dilatancy/compaction effect (D/C)  
 378 (solid lines), and the evolution effect (Evo) (dashed lines) in equation (21). The horizontal axis denotes time  
 379 normalized by the tidal cycle, and the values from 0 to 1 indicate one tidal cycle. The vertical axis denotes the tidal  
 380 Coulomb stress/frictional strength normalized by  $\sigma_{eff}^0$ . The numerical solutions for  $T_\theta/T = 14$  and  $U = 1$  are  
 381 shown in black, and those for  $T_\theta/T = 1.4$  and  $U = 0.01$  are shown in yellow.

382

## 383 4 Discussion

### 384 4.1 Application of the model to the observed tidal response during ETS

385 As mentioned in the introduction, most of the previous models are unable to account for the phase difference of  
 386  $\delta \sim \pi/2$ , which is observed at the early stage of ETS. In this section, we show that our model can reproduce the tidal  
 387 response during ETS, including the phase difference, for a specific range of fault physical properties. The obtained  
 388 range was compared with independent results from experiments, geological studies, and numerical modeling.

389 The observed tidal responses typically show  $\alpha \sim 0.1 \text{ kPa}^{-1}$  and  $\delta \sim \pi/2$  at the early stage of ETS and  $\alpha \sim 0.7 \text{ kPa}^{-1}$   
 390 and  $\delta \sim 0$  at the later stage of ETS. The slip velocity of the fault, which rapidly increases at the onset of ETS,  
 391 decreases to the steady-state subduction velocity with the progress of the ETS. In our model, ETS is represented by

392 setting  $V_{pl}$  higher than the steady-state subduction velocity (Table 2). We assume  $V_{pl} \sim 10^{-6}$  m/s at the early stage  
 393 of the ETS and  $V_{pl} \sim 10^{-8}$  m/s at the later stage, considering that  $V_{pl} \sim 10^{-8 \sim -6}$  m/s.

#### 394 4.2 The ranges of $U$ and $d_c$ reproduce the observation

395 We see from Figure 2a and 2b that the model reproduces the observed tidal response at the early stage of ETS  
 396 ( $\alpha \sim 0.1$ ,  $\delta \sim \pi/2$ ) when  $T_\theta/T \sim 10$  and  $U \sim 1$ . This case corresponds to the last of the three categories of  $T_\theta/T$   
 397 presented in Section 3.2.3. We have seen that the first term on the RHS of equation (21) (the dilatancy/compaction  
 398 effect term), which has a phase delay with respect to the tidal Coulomb stress change, dominates in the frictional  
 399 strength change, and  $\delta$  becomes  $\pi/2$ . The dominance of the dilatancy/compaction effect term reduces the direct  
 400 effect term, which results in a smaller variation in the slip velocity ( $\alpha \sim 0.1$ ). For  $V_{pl} = 10^{-6}$  m/s, we obtain  
 401  $d_c = 10^{-1}$  m from the condition of  $T_\theta/T \sim 10$  (equation (15)).

402 Up to this point, we have used the undrained model. The drained model assumes that the pore fluid pressure  
 403 diffuses outside the shear zone, as shown in equation (S1). This implies that the shear zone has a high permeability.  
 404 The drained model can reproduce  $\alpha$  for both the initial and later stages by assuming  $d_c = 10^{-2}$  m (the solid black  
 405 line in Figure S3a in the supporting information). However, the drained model cannot reproduce  $\delta \sim \pi/2$  at the early  
 406 stage (the solid black line in Figure S3b in the supporting information). The result that only the undrained model can  
 407 reproduce both  $\alpha$  and  $\delta$  suggests the low permeability of the shear zone. This indicates the possibility that our model  
 408 can constrain the frictional parameters and the dilatancy coefficient as well as a hydraulic property of the fault  
 409 through a comparison with observations of tidal response.

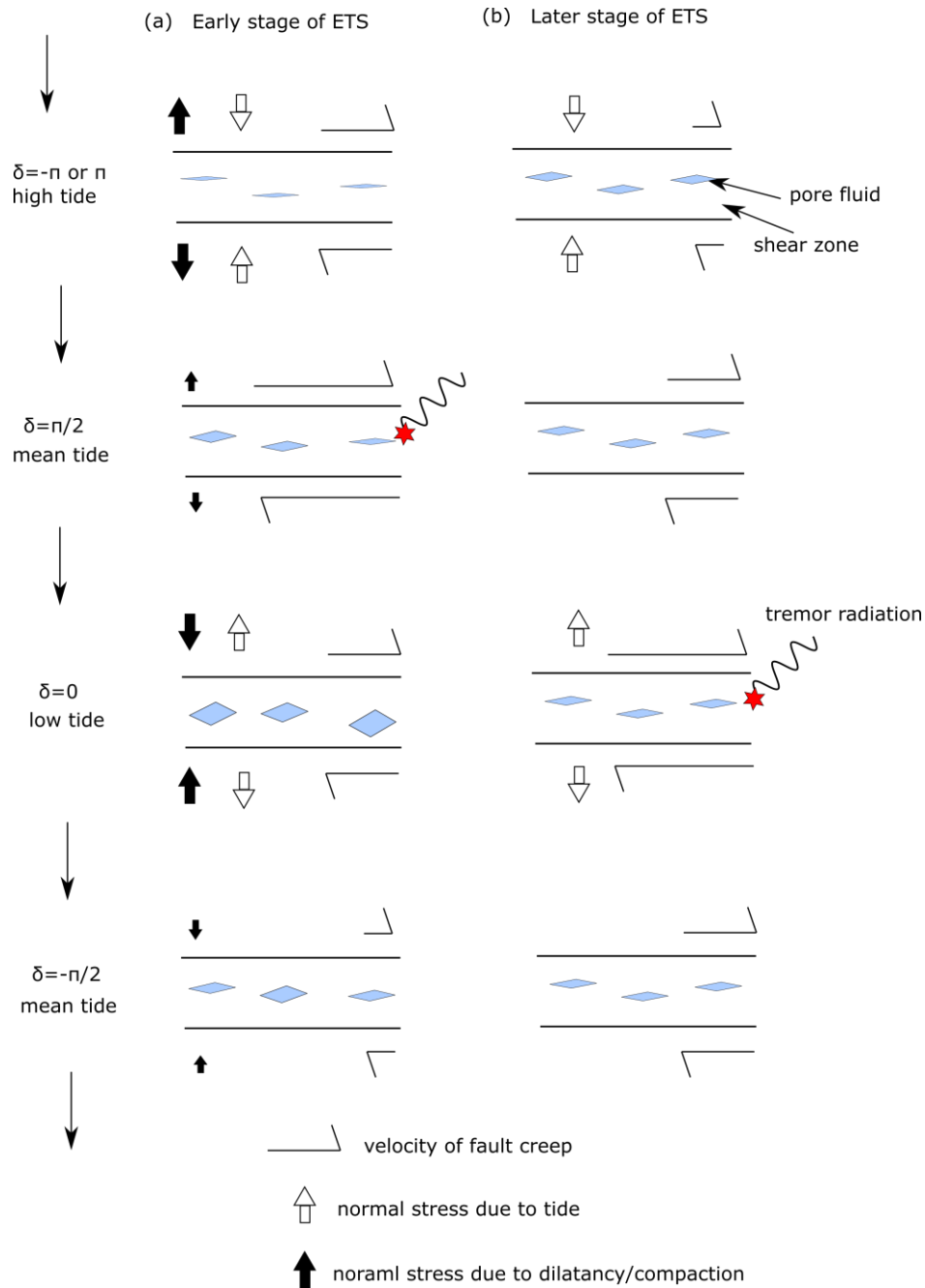
410 Now, we return to the application of the undrained model. Focusing on the case of  $U \sim 1$ , which explains the early  
 411 stage, we see that the model can reproduce the observed tidal response at the later stage of ETS ( $\alpha \sim 0.7$  kPa $^{-1}$  and  
 412  $\delta \sim 0$ ) when  $T_\theta/T \gtrsim 10^3$ . This case corresponds to  $T_\theta/T \gg |b - \mu_{pl}U|/a$  described in the three categories in  
 413 Section 3.2.3. As noted above, the phase advance disappears ( $\delta \sim 0$ ) as the direct effect term (second term) on the  
 414 RHS of equation (21) becomes dominant in the frictional strength change, and  $\alpha$  asymptotically reaches a value that  
 415 is independent of  $U$  ( $\alpha \sim 1/a\sigma_{eff}^0$ ). For  $V_{pl} = 10^{-8}$  m/s, the condition of  $T_\theta/T \gtrsim 10^3$  indicates that  $d_c \gtrsim 10^{-1}$  m.  
 416 On the other hand, Figure 2a shows that the model for  $U = 0.01$  and  $U = 0.1$  can explain the tidal response at the

417 later stage of ETS when  $d_c \gtrsim 10^{-3}$  m and  $d_c \gtrsim 10^{-2}$  m, respectively. This means that if we apply the model only  
418 to the tidal response at the later stage of ETS,  $d_c$  can be underestimated.

419 The above comparison between the model and observations shows that the dilatancy/compaction effect is dominant  
420 at the early stage of ETS, while the dilatancy/compaction effect is negligible at the later stage of ETS. Figure 4  
421 schematically illustrates the physical process suggested by our model. First, we see the early stage of ETS (Figure  
422 4a). A higher tide level increases the ocean load and reduces  $\Delta S(t)$ . At low tide ( $\delta \sim 0$ ),  $\Delta S(t)$  takes its maximum.  
423 However, the effect generated by the low tide is almost canceled out by the significant increase in the normal stress  
424 due to the dilatancy/compaction effect. At the mean tide ( $\delta \sim \pi/2$ ),  $\Delta S(t)$  is zero. The dilatancy/compaction effect is  
425 reduced but it still takes effect, decreasing the normal stress. Consequently, the slip velocity or the tremor rate  
426 reaches the maximum. Next, we see the later stage of ETS (Figure 4b). Since the dilatancy/compaction effect is  
427 always negligible at this stage, the slip velocity is maximized when  $\Delta S(t)$  becomes the largest (low tide).

428 Incidentally, we can reproduce the observed tidal response ( $\alpha, \delta$ ) as well as the observation that the number of  
429 tremors decreases by one or two orders of magnitude at the later stage of ETS compared to that at the early stage.  
430 This is obvious from the form of equation (2).

431



432

433 Figure 4. A schematic illustration of the relationship between the fault creep velocity and the tide level. For  
 434 simplicity, only the normal stress change is represented. (a) Early stage of ETS. The sum of the normal stress due to  
 435 the dilatancy/compaction effect (black arrows) and the tidal normal stress (white arrows) becomes the largest in the  
 436 sense of enhancing fault slip at  $\delta \sim \pi/2$ . (b) Later stage of ETS. The dilatancy/compaction effect is negligible, and  
 437 the fault creep velocity reaches its maximum at  $\delta \sim 0$ .

438

### 439 4.3 The constrained physical fault properties

440 For our model to simultaneously reproduce the observed tidal responses at the early and later stage of ETS, the  
 441 following four conditions must be satisfied:  $U(= M\epsilon/\sigma_{eff}^0) \sim 1$ ,  $d_c \sim 10^{-1}$  m, the occurrence of  
 442 dilatancy/compaction in the fault creep region (i.e.,  $a > b$ ) and low permeability within the shear zone (undrained  
 443 model). Below, we discuss the validity of these conditions.

#### 444 4.3.1 The dilatancy parameter $U$

445 Samuelson et al. (2009) obtained a dilatancy coefficient, and Segall et al. (1995) obtained bulk moduli of the fluid  
 446 and pore space. These results yield  $\epsilon \sim 10^{-4 \sim -5}$  and  $M \sim 10^{10}$  Pa (equation (7)). We assume that these experimentally  
 447 obtained values are of the same magnitude in the transition zone. Substituting these values into  $U(= \epsilon M/\sigma_{eff}^0) = 1$ ,  
 448 which reproduces the observed tidal response, we obtain  $\sigma_{eff}^0 = \epsilon M U \sim 10^{5 \sim 6}$  Pa, which supports a near-lithostatic  
 449 pore fluid pressure (e.g., Audet et al., 2009; Nakata, 2008; Shelly et al., 2006; Yabe et al., 2015).

#### 450 4.3.2 The critical slip distance $d_c$

451 The results of friction experiments on rocks and gouges show  $d_c \sim 10^{-4 \sim -6}$  m (e.g., Marone, 1998). Our results  
 452 ( $d_c \sim 10^{-1}$  m) are 3~5 orders of magnitude larger. The much larger critical slip distance can be explained by  
 453 considering the differences in roughness between laboratory surfaces and natural faults (Scholz et al., 1988) and the  
 454 differences in the thickness of the shear zone between experimental and natural faults (Marone and Kilgore, 1993).  
 455 Numerical models assuming the RSF also adopt a critical slip distance larger than that in the experimental results.  
 456 For example, Nakata et al. (2012) successfully modeled the SSE and aftershocks after the ~M7 earthquake in  
 457 Hyuga-nada, Japan, with  $d_c = 10^{-1 \sim 0}$  m. Maury et al. (2014) calculated a time evolution of shear stress for the SSE  
 458 in Mexico and estimated that the critical slip distance that can quantitatively reproduce the observed results is  
 459  $5 \times 10^{-2}$  m. Kawamura et al. (2018) applied a 1-D multidegree of freedom spring-slider model with  $d_c = 10^{-2}$  m  
 460 to reproduce various types of fault slip, such as fast slip, source nucleation, aftershock, and SSE. Our analysis of the  
 461 tidal response during ETS also supports  $d_c$  with the order of  $10^{-1}$  m.

## 462 4.3.3 The occurrence of dilatancy/compaction in the fault creep region

463 Numerical models that have been proposed thus far generally require the presence of a VW region ( $a - b < 0$ ) to  
 464 reproduce SSE (e.g., Liu and Rice, 2005; Segall et al., 2010). Some models have proposed a mechanism by which  
 465 SSE occurs in the VS regime, such as the generation of a negative Coulomb stress change due to fault valve action  
 466 (Perfettini and Ampuro 2008) and the transition of the RSF from the VW at low speeds to the VS at high speeds  
 467 (e.g., Im et al., 2020; Peng and Rubin, 2018; Shibazaki and Iio, 2003). Our model employs the framework of the VS  
 468 and expresses the velocity of the slow slip by  $V_{pl}$  phenomenologically.

469 The above two models assuming the VS (e.g., Im et al., 2020; Peng and Rubin, 2018; Perfettini and Ampuro, 2008;  
 470 Shibazaki and Iio 2003) do not consider the time variation of pore fluid pressure. On the other hand, Beeler et al.  
 471 (2018) developed a model that considers the time variation of pore fluid pressure in the VW region. However, it  
 472 cannot explain the tidal response at the early stage of ETS. Our results show that when we assume the framework of  
 473 the VS, the observed tidal response at the early stage of ETS cannot be reproduced unless dilatancy/compaction  
 474 occurs.

## 475 4.3.4 The fluid pressure diffusivity derived from the undrained condition

476 Our results support the undrained model (Section 4.2). For the undrained model,  $T \ll t_w$  must be satisfied (Section  
 477 2.2.2). Using this condition, we can quantitatively constrain the fluid pressure diffusivity as follows. We assume that  
 478 the thickness of the shear zone is  $w$  and the fluid pressure diffusivity in the shear zone is  $c_{hyd}^*$ . Then, a dimensional  
 479 analysis shows that  $w \sim \sqrt{t_w c_{hyd}^*}$ , where  $t_w$  denotes the characteristic timescale on which the pore fluid pressure  
 480 diffuses through the shear zone. Therefore, the condition of  $T \ll t_w$  can be rewritten as  $T \ll w^2 / c_{hyd}^*$ .

481 We estimate  $w$  in the transition zone in the following manner, since it cannot be observed directly. A drilling  
 482 investigation and structural analyses of drill cores on the Nojima Fault revealed that  $w$  in the seismogenic zone is  
 483  $\sim 10^{1/2}$  m (Lin and Nishikawa, 2019). It is generally expected that  $w$  in the VS region is larger than in the VW  
 484 region (e.g., Chen and Rampel, 2015). Therefore, we assume  $w \sim 10^{0 \sim 1/2}$  m in the VS region. Then, the above  
 485 undrained condition yields  $c_{hyd}^* \ll 2 * 10^{-5 \sim -4}$  m<sup>2</sup>/s. Previous studies have shown that the  $c_{hyd}^*$  of the seismogenic  
 486 zone is  $\sim 10^{-8 \sim -3}$  m<sup>2</sup>/s (Yamashita and Tsutsumi, 2018). Our results suggest that the shear zone in the transition  
 487 zone is probably as impermeable as that in the seismogenic zone.

## 488           4.4 Other effects than dilatancy/compaction

489       We have seen that the dilatancy/compaction effect is important to explain the phase difference ( $\delta \sim \pi/2$ ) in the tidal  
490 response. In this section, we examine whether other effects could explain  $\delta \sim \pi/2$ . The following possibilities are  
491 considered.

492       (I) Change in the tidal period  $T$  as in Ader et al. (2012). In this case,  $\delta \sim \pi/2$  can be realized when  $T >$   
493  $O(10^9 \sim 10^{10}$  s), regardless of the critical slip distance. However, such a  $T$  value exceeds the longest tidal period (18.6  
494 years).

495       (II) Introduction of a change in the state variable due to the normal stress acting on the fault plane (Linker and  
496 Dieterich, 1992). In this case, the time variation of the state variable can be written as follows:

$$\frac{d\theta}{dt} = -\frac{V\theta}{d_c} \log\left(\frac{V\theta}{d_c}\right) - \frac{\gamma \dot{\sigma}}{b\sigma} \theta, \#(23)$$

497       where  $\gamma$  is a constitutive parameter representing a normal stress dependence. In general,  $\gamma \sim O(0.1)$ . Therefore, we  
498 adopt  $\gamma = 0.2$  and solve the governing equations of our model replacing the evolution law (equation (4)) with  
499 equation (23). The results indicate that the difference caused by considering the effect of normal stress on the state  
500 variable is less than 1%. Therefore, the influence of the Linker-Dieterich effect is small and does not provide a  
501 reason for the large phase difference.

502       (III) Tidal Coulomb stress can directly destroy the tremor source instead of aseismic slip on the surrounding fault.  
503 This effect is ignored in our model. If this is the case, the tremor rate is proportional to the tidal Coulomb stressing  
504 rate (i.e.,  $\delta \sim \pi/2$ ) (Beeler et al., 2013; Lockner and Beeler, 1999). This direct effect of the tidal Coulomb stress  
505 should become clearer when the aseismic slip on the surrounding fault is smaller, i.e., at the later stage of ETS  
506 (Royer et al., 2015). However, the observed result shows  $\delta \sim 0$  at the later stage, indicating that the direct effect is  
507 smaller.

508       None of the above effects can explain the phase difference of  $\delta \sim \pi/2$ , and thus the pore fluid pressure change due  
509 to dilatancy/compaction is more likely to cause the large phase difference at the early stage of ETS.

## 510           4.5 Application to the tidal response of continuous families

511       By setting the value of  $V_{pl}$  to a steady-state plate convergence velocity (e.g.,  $10^{-9}$  m/s), we can examine the range  
512 of  $d_c$  and  $U$  in which our model reproduces the tidal response of continuous families. The observations show that

513 the tidal response of continuous families is  $\delta \sim 0$  (Ide and Tanaka, 2014; Thomas et al., 2012) and  $\alpha \sim 1.5 \text{ kPa}^{-1}$   
 514 (Thomas et al., 2012), for example. We examine whether these observations can be reproduced with parameters that  
 515 reproduce the tidal response of episodic families ( $d_c \sim 10^{-1} \text{ m}$ ,  $U \sim 1$ ) (Section 4.2). In the case of  $d_c = 10^{-1} \text{ m}$ ,  
 516  $V_{pl} = 10^{-9} \text{ m/s}$  and  $T_\theta/T \sim 10^4$ , we obtain  $\alpha \sim a\sigma_{eff}^0 (= 0.67 \text{ kPa}^{-1})$  and  $\delta \sim 0$  (Section 3.2.2). Therefore, by  
 517 slightly reducing the value of  $\sigma_{eff}^0$ , the tidal responses of continuous families and episodic families can be  
 518 reproduced with similar values of the fault physical properties.

#### 519 4.6 Limitations of our model

520 Because our model adopts a one-degree-of-freedom (one-DOF) spring-slider system, it cannot simulate the  
 521 spatiotemporal variation in stress during ETS. Such spatiotemporal changes in stress have been modeled using a  
 522 two-dimensional system (e.g., Hawthorne and Rubin, 2013), which can reproduce observations such as a spatial  
 523 propagation of ETS and temporal changes in the slip velocity during ETS. Hawthorne and Rubin (2013) examined  
 524 the tidal response of ETS based on such a 2-D model.

525 However, Hawthorne and Rubin (2013) reported that the tidal response during ETS obtained by a 2-D simulation  
 526 qualitatively agrees with the tidal response of the one-DOF ramp block slider model. Their model does not include  
 527 the effect of dilatancy/compaction. To confirm whether the one-DOF and 2-D simulation results are in agreement  
 528 for a model including the dilatancy/compaction effect, we need to extend our model to a 2-D system. One approach  
 529 to do so would be to incorporate the dilatancy/compaction effect considered in our model into the model of  
 530 Hawthorne and Rubin (2013).

### 531 5 Conclusions

532 Tremors in the transition zone are sensitive to tidal stress. In this study, we propose a physical model to explain the  
 533 tidal response of tremors observed during ETS. Following previous studies (Ader et al., 2012; Beeler et al., 2013;  
 534 Shelly et al., 2007a), we assumed that tremors are generated by the rupture of a small brittle patch on the fault plane  
 535 due to the aseismic shear slip of a larger-scale surrounding fault. As in Ader et al. (2012), we adopted a one-degree-  
 536 of-freedom spring-slider that follows the RSF for the VS and set up the governing equations to describe the slip  
 537 behavior of the block, considering a pore fluid pressure change in the shear zone (Section 2). The inclusion of pore

538 pressure changes due to dilatancy/compaction in the VS regime is a remarkable contrast to previous theoretical  
 539 models describing tidal modulation.

540 In our model, the tidal response is expressed with the tidal sensitivity ( $\alpha$ ), which represents the amplitude of the  
 541 tidal modulation of fault creep velocity, and the phase difference ( $\delta$ ) of the fault creep velocity peak relative to the  
 542 tidal Coulomb stress peak. We analytically derived an approximate solution to reveal how the tidal response depends  
 543 on the fault physical properties in Section 3. We note that the slip behavior is primarily controlled by the  
 544 characteristic timescale  $T_\theta (= 2\pi d_c/V_{pl})$  at which the state variable evolves, where  $d_c$  is the critical slip distance  
 545 and  $V_{pl}$  is the background fault creep. We found that the behavior of  $\alpha$  and  $\delta$  can be classified into three cases  
 546 according to the magnitude of  $T_\theta/T$  ( $T_\theta/T \gg |b - \mu_{pl}U|/a$ ,  $T_\theta/T \sim |b - \mu_{pl}U|/a$ ,  $T_\theta/T \ll 1$ ), where  $T$  is the  
 547 tidal cycle ( $\sim 12$  hours),  $a$  and  $b$  are frictional constitutive parameters,  $\mu_{pl}$  is the frictional coefficient and  $U$  is the  
 548 dilatancy parameter. This classification reflects the degree to which the dilatancy/compaction effect is dominant in  
 549 the frictional strength change. We showed that the smaller  $T_\theta/T$  is, the more dominant the dilatancy/compaction  
 550 effect is in the friction strength change.

551 We applied the model to ETS, assuming that  $V_{pl}$  changes between the early and later stages of the ETS. The model  
 552 successfully reproduced the tidal response observed at both stages of the ETS. We constrained the effective normal  
 553 stress to be  $10^{5\sim 6}$  Pa, the critical slip distance to be  $10^{-1}$  m, and the fluid pressure diffusivity to be  $10^{-5}$  m<sup>2</sup>/s or  
 554 less. Of particular importance is the use of the phase difference in the estimation of the fault properties. Without  
 555 considering the dilatancy/compaction effect, the phase difference at the early stage cannot be reproduced. Moreover,  
 556 using the tidal response data obtained during only the early stage or the later stage produces different estimates of  
 557 the fault properties. The range of the fault properties obtained in our study are in the ranges inferred by independent  
 558 studies. Our model supports a critical slip distance of  $\sim 10^{-1}$  m, which has been used in numerical simulations of  
 559 earthquake cycles. This study shows that the physical modeling of the tidal response of tremors during ETS is an  
 560 effective method to retrieve the fault properties in the transition zone, including hydraulic properties.

561

562 **Appendix**

563 **Appendix A: Derivation of equation (21)**

564 Substituting equation (3) into equation (8) and transforming the result, we obtain

$$\begin{aligned}
 k\Delta u + \Delta\tau &= \left\{ \mu_0 + a \log\left(\frac{V_{pl}}{V_0}\right) + b \log\left(\frac{\theta_{pl}}{\theta_0}\right) + a \log\left(\frac{V}{V_{pl}}\right) + b \log\left(\frac{\theta}{\theta_{pl}}\right) \right\} \sigma_{eff} \\
 &= \left\{ \mu_{pl} + a \log\left(\frac{V}{V_{pl}}\right) + b \log\left(\frac{\theta}{\theta_{pl}}\right) \right\} \sigma_{eff}. \#(A)
 \end{aligned}$$

565 We represent the relative displacement of the block at the steady state without the tide as  $\Delta u_{no}$ . Then,  $k\Delta u_{no} =$   
 566  $\mu_{pl}\sigma_{eff}^0$  holds, where the RHS is obtained by setting  $\Delta\sigma(t) = 0$  and  $\Delta p(t) = 0$  in equation (9). We can confirm that  
 567  $k\Delta u \sim \mu_{pl}\sigma_{eff}^0$  as follows. For the parameter set in Table 2,  $k\Delta\dot{u} \sim O(kV_{pl})$  is three orders of magnitude smaller than  
 568  $\Delta\dot{\tau} \sim O(2\pi|\Delta\tau|/T)$ . This means that  $k\Delta\dot{u}$  on the LHS of the time derivative of equation (A) is negligibly small,  
 569 suggesting that  $\Delta u \sim \Delta u_{no}$ . Replacing  $k\Delta u$  with  $\mu_{pl}\sigma_{eff}^0$  on the LHS and using equations (9) and (11), equation (A)  
 570 can be rewritten as

$$\Delta S(t) = -\mu_{pl}\Delta p(t) + a\sigma_{eff}\log\left(\frac{V}{V_{pl}}\right) + b\sigma_{eff}\log\left(\frac{\theta}{\theta_{pl}}\right). \#(B)$$

571 In equation (B), the LHS corresponds to the tidal Coulomb stress and the RHS corresponds to the frictional strength.  
 572 Furthermore, equation (B) can be written as

$$\Delta S(t) \sim -\mu_{pl}U\sigma_{eff}^0\log\left(\frac{\theta}{\theta_{pl}}\right) + a\sigma_{eff}^0\log\left(\frac{V}{V_{pl}}\right) + b\sigma_{eff}^0\log\left(\frac{\theta}{\theta_{pl}}\right) \#(C)$$

574 by using equation (7), where  $\Delta p = 0$  is taken at  $\theta = \theta_{pl}$ , and it is assumed that the changes in the effective normal  
 575 stress in the second and third terms on the RHS of equation (C) are sufficiently small compared to  $\sigma_{eff}^0$ .

577 **Appendix B: Derivation of equation (22)**

578 Substituting  $-\mu_{pl}U\sigma_{eff}^0\log(\theta/\theta_{pl}) \sim \Delta S e^{i\omega(t-\beta)}$  and  $b\sigma_{eff}^0\log(\theta/\theta_{pl}) \sim 0$  into equation (21), as described in Section  
 579 3.2.3, we obtain

$$\log\left(\frac{V}{V_{pl}}\right) \sim |\Delta S(t)| \text{Re}(e^{i\omega t} - e^{i\omega(t-\beta)}). \#(D)$$

580 When  $\theta_1 = \omega t - \beta/2, \theta_2 = \beta/2$ , we can write  $Re(e^{i\omega t} - e^{i\omega(t-\beta)}) = \cos(\theta_1 + \theta_2) - \cos(\theta_1 - \theta_2) =$   
 581  $\sin(\theta_1) \sin(\theta_2)$ . Using  $\sin(\theta_1) = \cos(\pi/2 + \theta_1)$ , we obtain  $\sin(\theta_1) \sin(\theta_2) = \cos(\omega t + (\pi - \beta)/2) \sin(\beta/2)$ .  
 582 That is,  $\log(V/V_{pl}) \sim |\Delta S(t)| \sin(\beta/2) \cos(\omega t + (\pi - \beta)/2)$ . Furthermore, since  $\beta \ll \pi$ , equation (D) can be  
 583 rewritten as

$$\log\left(\frac{V}{V_{pl}}\right) \sim |\Delta S(t)| \sin\left(\frac{\beta}{2}\right) \operatorname{Re}\left\{e^{i\left(\omega t + \frac{\pi}{2}\right)}\right\}. \#(E)$$

584

## 585 **Acknowledgments**

586 We acknowledge Dr. Takehito Suzuki for the valuable discussion. For this study, we used the computer systems of  
 587 the Earthquake and Volcano Information Center of the Earthquake Research Institute, The University of Tokyo.  
 588 This work was supported by JSPS KAKENHI Grant Numbers JP16H02219, JP16H06474, JP21H01187 and  
 589 JP21H05204.

## 590 **References**

- 591 Ader, T. J., Ampuero, J. P., & Avouac, J. P. (2012). The role of velocity-neutral creep on the modulation of tectonic  
 592 tremor activity by periodic loading. *Geophysical research letters*, *39*(16). <https://doi.org/10.1029/2012GL052326>
- 593 Audet, P., Bostock, M. G., Christensen, N. I., & Peacock, S. M. (2009). Seismic evidence for overpressured  
 594 subducted oceanic crust and megathrust fault sealing. *Nature*, *457*(7225), 76-78.  
 595 <https://doi.org/10.1038/nature07650>
- 596 Audet, P., & Bürgmann, R. (2014). Possible control of subduction zone slow-earthquake periodicity by silica  
 597 enrichment. *Nature*, *510*(7505), 389-392. <https://doi.org/10.1038/nature13391>
- 598 Bartlow, N. M., Miyazaki, S. I., Bradley, A. M., & Segall, P. (2011). Space-time correlation of slip and tremor  
 599 during the 2009 Cascadia slow slip event. *Geophysical Research Letters*, *38*(18).  
 600 <https://doi.org/10.1029/2011GL048714>
- 601 Beeler, N. M., Thomas, A., Bürgmann, R., & Shelly, D. (2013). Inferring fault rheology from low-frequency  
 602 earthquakes on the San Andreas. *Journal of Geophysical Research: Solid Earth*, *118*(11), 5976-5990.  
 603 <https://doi.org/10.1002/2013JB010118>

- 604 Beeler, N. M., Thomas, A., Bürgmann, R., & Shelly, D. (2018). Constraints on friction, dilatancy, diffusivity, and  
605 effective stress from low-frequency earthquake rates on the deep San Andreas Fault. *Journal of Geophysical*  
606 *Research: Solid Earth*, 123(1), 583-605. <https://doi.org/10.1002/2017JB015052>
- 607 Chen, J., & Rempel, A. W. (2015). Shear zone broadening controlled by thermal pressurization and poroelastic  
608 effects during model earthquakes. *Journal of Geophysical Research: Solid Earth*, 120(7), 5215-5237.  
609 <https://doi.org/10.1002/2014JB011641>
- 610 Chen, K. H., Tai, H. J., Ide, S., Byrne, T. B., & Johnson, C. W. (2018). Tidal modulation and tectonic implications  
611 of tremors in Taiwan. *Journal of Geophysical Research: Solid Earth*, 123(7), 5945-5964.  
612 <https://doi.org/10.1029/2018JB015663>
- 613 Dieterich, J. H. (1979). Modeling of rock friction: 1. Experimental results and constitutive equations. *Journal of*  
614 *Geophysical Research: Solid Earth*, 84(B5), 2161-2168. <https://doi.org/10.1029/JB084iB05p02161>
- 615 Dragert, H., Wang, K., & James, T. S. (2001). A silent slip event on the deeper Cascadia subduction  
616 interface. *Science*, 292(5521), 1525-1528. <https://doi.org/10.1126/science.1060152>
- 617 Hawthorne, J. C., & Rubin, A. M. (2013). Tidal modulation and back-propagating fronts in slow slip events  
618 simulated with a velocity-weakening to velocity-strengthening friction law. *Journal of Geophysical Research: Solid*  
619 *Earth*, 118(3), 1216-1239. <https://doi.org/10.1002/jgrb.50107>
- 620 Hirose, H., Hirahara, K., Kimata, F., Fujii, N., & Miyazaki, S. I. (1999). A slow thrust slip event following the two  
621 1996 Hyuganada earthquakes beneath the Bungo Channel, southwest Japan. *Geophysical Research Letters*, 26(21),  
622 3237-3240. <https://doi.org/10.1029/1999GL010999>
- 623 Hirose, H., & Obara, K. (2010). Recurrence behavior of short-term slow slip and correlated nonvolcanic tremor  
624 episodes in western Shikoku, southwest Japan. *Journal of Geophysical Research: Solid Earth*, 115(B6).  
625 <https://doi.org/10.1029/2008JB006050>
- 626 Houston, H. (2015). Low friction and fault weakening revealed by rising sensitivity of tremor to tidal stress. *Nature*  
627 *Geoscience*, 8(5), 409-415. <https://doi.org/10.1038/ngeo2419>
- 628 Ide, S. (2010). Striations, duration, migration and tidal response in deep tremor. *Nature*, 466(7304), 356-359.  
629 <https://doi.org/10.1038/nature09251>

- 630 Ide, S., Shelly, D. R., & Beroza, G. C. (2007). Mechanism of deep low frequency earthquakes: Further evidence that  
631 deep non-volcanic tremor is generated by shear slip on the plate interface. *Geophysical Research Letters*, *34*(3).  
632 <https://doi.org/10.1029/2006GL028890>
- 633 Ide, S., & Tanaka, Y. (2014). Controls on plate motion by oscillating tidal stress: Evidence from deep tremors in  
634 western Japan. *Geophysical Research Letters*, *41*(11), 3842-3850. <https://doi.org/10.1002/2014GL060035>
- 635 Ide, S., Yabe, S., Tai, H. J., & Chen, K. H. (2015). Thrust-type focal mechanisms of tectonic tremors in Taiwan:  
636 Evidence of subduction. *Geophysical Research Letters*, *42*(9), 3248-3256. <https://doi.org/10.1002/2015GL063794>
- 637 Ide, S., Yabe, S., & Tanaka, Y. (2016). Earthquake potential revealed by tidal influence on earthquake size–  
638 frequency statistics. *Nature Geoscience*, *9*(11), 834-837. <https://doi.org/10.1038/ngeo2796>
- 639 Im, K., Saffer, D., Marone, C., & Avouac, J. P. (2020). Slip-rate-dependent friction as a universal mechanism for  
640 slow slip events. *Nature Geoscience*, *13*(10), 705-710. <https://doi.org/10.1038/s41561-020-0627-9>
- 641 Ito, Y., Obara, K., Shiomi, K., Sekine, S., & Hirose, H. (2007). Slow earthquakes coincident with episodic tremors  
642 and slow slip events. *Science*, *315*(5811), 503-506. <https://doi.org/10.1126/science.1134454>
- 643 Kawamura, H., Yamamoto, M., & Ueda, Y. (2018). Slow-Slip Phenomena Represented by the One-Dimensional  
644 Burridge–Knopoff Model of Earthquakes. *Journal of the Physical Society of Japan*, *87*(5), 053001.  
645 <https://doi.org/10.7566/JPSJ.87.053001>
- 646 Lin, A., & Nishiwaki, T. (2019). Repeated seismic slipping events recorded in a fault gouge zone: Evidence from  
647 the Nojima fault drill holes, SW Japan. *Geophysical Research Letters*, *46*(3), 1276-1283.  
648 <https://doi.org/10.1029/2019GL081927>
- 649 Linker, M. F., & Dieterich, J. H. (1992). Effects of variable normal stress on rock friction: Observations and  
650 constitutive equations. *Journal of Geophysical Research: Solid Earth*, *97*(B4), 4923-4940.  
651 <https://doi.org/10.1029/92JB00017>
- 652 Liu, Y. (2013). Numerical simulations on megathrust rupture stabilized under strong dilatancy strengthening in slow  
653 slip region. *Geophysical Research Letters*, *40*(7), 1311-1316. <https://doi.org/10.1002/grl.50298>
- 654 Liu, Y., & Rice, J. R. (2005). Aseismic slip transients emerge spontaneously in three-dimensional rate and state  
655 modeling of subduction earthquake sequences. *Journal of Geophysical Research: Solid Earth*, *110*(B8).  
656 <https://doi.org/10.1029/2004JB003424>

- 657 Luo, Y., & Ampuero, J. P. (2018). Stability of faults with heterogeneous friction properties and effective normal  
658 stress. *Tectonophysics*, 733, 257-272. <https://doi.org/10.1016/j.tecto.2017.11.006>
- 659 Luo, Y., & Liu, Z. (2019). Rate-and-state model casts new insight into episodic tremor and slow-slip variability in  
660 Cascadia. *Geophysical Research Letters*, 46(12), 6352-6362. <https://doi.org/10.1029/2019GL082694>
- 661 Matsuzawa, T., Hirose, H., Shibazaki, B., & Obara, K. (2010). Modeling short-and long-term slow slip events in the  
662 seismic cycles of large subduction earthquakes. *Journal of Geophysical Research: Solid Earth*, 115(B12).  
663 <https://doi.org/10.1029/2010JB007566>
- 664 Marone, C. (1998). Laboratory-derived friction laws and their application to seismic faulting. *Annual Review of*  
665 *Earth and Planetary Sciences*, 26(1), 643-696. <https://doi.org/10.1146/annurev.earth.26.1.643>
- 666 Marone, C., & Kilgore, B. (1993). Scaling of the critical slip distance for seismic faulting with shear strain in fault  
667 zones. *Nature*, 362(6421), 618-621. <https://doi.org/10.1038/362618a0>
- 668 Marone, C., Raleigh, C. B., & Scholz, C. H. (1990). Frictional behavior and constitutive modeling of simulated fault  
669 gouge. *Journal of Geophysical Research: Solid Earth*, 95(B5), 7007-7025.  
670 <https://doi.org/10.1029/JB095iB05p07007>
- 671 Maury, J., Aochi, H., & Radiguet, M. (2014). Fault constitutive relations inferred from the 2009-2010 slow slip  
672 event in Guerrero, Mexico. *Geophysical Research Letters*, 41(14), 4929-4936.  
673 <https://doi.org/10.1002/2014GL060691>
- 674 Meade, B. J., & Loveless, J. P. (2009). Predicting the geodetic signature of  $M_w \geq 8$  slow slip events. *Geophysical*  
675 *Research Letters*, 36(1). <https://doi.org/10.1029/2008GL036364>
- 676 Métivier, L., de Viron, O., Conrad, C. P., Renault, S., Diament, M., & Patau, G. (2009). Evidence of earthquake  
677 triggering by the solid earth tides. *Earth and Planetary Science Letters*, 278(3-4), 370-375.  
678 <https://doi.org/10.1016/j.epsl.2008.12.024>
- 679 Mizoguchi, K., Hirose, T., Shimamoto, T., & Fukuyama, E. (2008). Internal structure and permeability of the  
680 Nojima fault, southwest Japan. *Journal of Structural Geology*, 30(4), 513-524.  
681 <https://doi.org/10.1016/j.jsg.2007.12.002>
- 682 Nakata, R., Hyodo, M., & Hori, T. (2012). Numerical simulation of afterslips and slow slip events that occurred in  
683 the same area in Hyuga-nada of southwest Japan. *Geophysical Journal International*, 190(2), 1213-1220.  
684 <https://doi.org/10.1111/j.1365-246X.2012.05552.x>

- 685 Nakata, R., Suda, N., & Tsuruoka, H. (2008). Nonvolcanic tremor resulting from the combined effect of Earth tides  
686 and slow slip events. *Nature Geoscience*, *1*(10), 676-678. <https://doi.org/10.1038/ngeo288>
- 687 Obara, K. (2002). Nonvolcanic deep tremor associated with subduction in southwest Japan. *Science*, *296*(5573),  
688 1679-1681. <https://doi.org/10.1126/science.1070378>
- 689 Obara, K., Hirose, H., Yamamizu, F., & Kasahara, K. (2004). Episodic slow slip events accompanied by non-  
690 volcanic tremors in southwest Japan subduction zone. *Geophysical Research Letters*, *31*(23).  
691 <https://doi.org/10.1029/2004GL020848>
- 692 Peng, Y., & Rubin, A. M. (2018). Simulating Short-Term Evolution of Slow Slip Influenced by Fault  
693 Heterogeneities and Tides. *Geophysical Research Letters*, *45*(19), 10-269. <https://doi.org/10.1029/2018GL078752>
- 694 Perfettini, H., & Ampuero, J. P. (2008). Dynamics of a velocity strengthening fault region: Implications for slow  
695 earthquakes and postseismic slip. *Journal of Geophysical Research: Solid Earth*, *113*(B9).  
696 <https://doi.org/10.1029/2007JB005398>
- 697 Perfettini, H., & Schmittbuhl, J. (2001). Periodic loading on a creeping fault: Implications for tides. *Geophysical*  
698 *Research Letters*, *28*(3), 435-438. <https://doi.org/10.1029/2000GL011686>
- 699 Proctor, B., Lockner, D. A., Kilgore, B. D., Mitchell, T. M., & Beeler, N. M. (2020). Direct evidence for fluid  
700 pressure, dilatancy, and compaction affecting slip in isolated faults. *Geophysical Research Letters*, *47*(16).  
701 <https://doi.org/10.1029/2019GL086767>
- 702 Rice, J. R. (2006). Heating and weakening of faults during earthquake slip. *Journal of Geophysical Research: Solid*  
703 *Earth*, *111*(B5). <https://doi.org/10.1029/2005JB004006>
- 704 Rogers, G., & Dragert, H. (2003). Episodic tremor and slip on the Cascadia subduction zone: The chatter of silent  
705 slip. *Science*, *300*(5627), 1942-1943. <https://doi.org/10.1126/science.1084783>
- 706 Royer, A. A., Thomas, A. M., & Bostock, M. G. (2015). Tidal modulation and triggering of low-frequency  
707 earthquakes in northern Cascadia. *Journal of Geophysical Research: Solid Earth*, *120*(1), 384-405.  
708 <https://doi.org/10.1002/2014JB011430>
- 709 Rubinstein, J. L., La Rocca, M., Vidale, J. E., Creager, K. C., & Wech, A. G. (2008). Tidal modulation of  
710 nonvolcanic tremor. *Science*, *319*(5860), 186-189. <https://doi.org/10.1126/science.1150558>
- 711 Ruina, A. (1983). Slip instability and state variable friction laws. *Journal of Geophysical Research: Solid*  
712 *Earth*, *88*(B12), 10359-10370. <https://doi.org/10.1029/JB088iB12p10359>

- 713 Samuelson, J., Elsworth, D., & Marone, C. (2009). Shear-induced dilatancy of fluid-saturated faults: Experiment and  
714 theory. *Journal of Geophysical Research: Solid Earth*, 114(B12). <https://doi.org/10.1029/2008JB006273>
- 715 Scholz, C. H. (1988). The critical slip distance for seismic faulting. *Nature*, 336(6201), 761-763.  
716 <https://doi.org/10.1038/336761a0>
- 717 Scholz, C. H. (1998). Earthquakes and friction laws. *Nature*, 391(6662), 37-42. <https://doi.org/10.1038/34097>
- 718 Scholz, C. H. (2019). *The mechanics of earthquakes and faulting*. New York, NY; Cambridge University Press.  
719 <https://doi.org/10.1017/9781316681473>
- 720 Scholz, C. H., Tan, Y. J., & Albino, F. (2019). The mechanism of tidal triggering of earthquakes at mid-ocean  
721 ridges. *Nature communications*, 10(1), 1-7. <https://doi.org/10.1038/s41467-019-10605-2>
- 722 Schwartz, S. Y., & Rokosky, J. M. (2007). Slow slip events and seismic tremor at circum-Pacific subduction  
723 zones. *Reviews of Geophysics*, 45(3). <https://doi.org/10.1029/2006RG000208>
- 724 Segall, P. (2010). *Earthquake and volcano deformation*. Princeton NJ: Princeton University Press.  
725 <https://doi.org/10.1515/9781400833856>
- 726 Segall, P., & Rice, J. R. (1995). Dilatancy, compaction, and slip instability of a fluid-infiltrated fault. *Journal of*  
727 *Geophysical Research: Solid Earth*, 100(B11), 22155-22171. <https://doi.org/10.1029/95JB02403>
- 728 Segall, P., Rubin, A. M., Bradley, A. M., & Rice, J. R. (2010). Dilatant strengthening as a mechanism for slow slip  
729 events. *Journal of Geophysical Research: Solid Earth*, 115(B12). <https://doi.org/10.1029/2010JB007449>
- 730 Shelly, D. R., Beroza, G. C., & Ide, S. (2007a). Non-volcanic tremor and low-frequency earthquake  
731 swarms. *Nature*, 446(7133), 305-307. <https://doi.org/10.1038/nature05666>
- 732 Shelly, D. R., Beroza, G. C., & Ide, S. (2007b). Complex evolution of transient slip derived from precise tremor  
733 locations in western Shikoku, Japan. *Geochemistry, Geophysics, Geosystems*, 8(10).  
734 <https://doi.org/10.1029/2007GC001640>
- 735 Shelly, D. R., Beroza, G. C., Ide, S., & Nakamura, S. (2006). Low-frequency earthquakes in Shikoku, Japan, and  
736 their relationship to episodic tremor and slip. *Nature*, 442(7099), 188-191. <https://doi.org/10.1038/nature04931>
- 737 Shelly, D. R., Peng, Z., Hill, D. P., & Aiken, C. (2011). Triggered creep as a possible mechanism for delayed  
738 dynamic triggering of tremor and earthquakes. *Nature Geoscience*, 4(6), 384-388. <https://doi.org/10.1038/ngeo1141>
- 739 Shibazaki, B., & Iio, Y. (2003). On the physical mechanism of silent slip events along the deeper part of the  
740 seismogenic zone. *Geophysical Research Letters*, 30(9). <https://doi.org/10.1029/2003GL017047>

- 741 Shibazaki, B., Obara, K., Matsuzawa, T., & Hirose, H. (2012). Modeling of slow slip events along the deep  
742 subduction zone in the Kii Peninsula and Tokai regions, southwest Japan. *Journal of Geophysical Research: Solid*  
743 *Earth*, 117(B6). <https://doi.org/10.1029/2011JB009083>
- 744 Suzuki, T., & Yamashita, T. (2009). Dynamic modeling of slow earthquakes based on thermoporoelastic effects and  
745 inelastic generation of pores. *Journal of Geophysical Research: Solid Earth*, 114(B6).  
746 <https://doi.org/10.1029/2008JB006042>
- 747 Tan, Y. J., & Marsan, D. (2020). Connecting a broad spectrum of transient slip on the San Andreas fault. *Science*  
748 *advances*, 6(33), eabb2489. <https://doi.org/10.1126/sciadv.abb2489>
- 749 Thomas, A. M., Beeler, N. M., Bletery, Q., Burgmann, R., & Shelly, D. R. (2018). Using low-frequency earthquake  
750 families on the San Andreas Fault as deep creepmeters. *Journal of Geophysical Research: Solid Earth*, 123(1), 457-  
751 475. <https://doi.org/10.1002/2017JB014404>
- 752 Thomas, A. M., Bürgmann, R., Shelly, D. R., Beeler, N. M., & Rudolph, M. L. (2012). Tidal triggering of low  
753 frequency earthquakes near Parkfield, California: Implications for fault mechanics within the brittle-ductile  
754 transition. *Journal of Geophysical Research: Solid Earth*, 117(B5). <https://doi.org/10.1029/2011JB009036>
- 755 Thomas, A. M., Nadeau, R. M., & Bürgmann, R. (2009). Tremor-tide correlations and natthostatic pore pressure on  
756 the deep San Andreas fault. *Nature*, 462(7276), 1048-1051. <https://doi.org/10.1038/nature08654>
- 757 van der Elst, N. J., Delorey, A. A., Shelly, D. R., & Johnson, P. A. (2016). Fortnightly modulation of San Andreas  
758 tremor and low-frequency earthquakes. *Proceedings of the National Academy of Sciences*, 113(31), 8601-8605.  
759 <https://doi.org/10.1073/pnas.1524316113>
- 760 Vidale, J. E., Agnew, D. C., Johnston, M. J., & Oppenheimer, D. H. (1998). Absence of earthquake correlation with  
761 Earth tides: An indication of high preseismic fault stress rate. *Journal of Geophysical Research: Solid*  
762 *Earth*, 103(B10), 24567-24572. <https://doi.org/10.1029/98JB00594>
- 763 Villafuerte, C., & Cruz-Atienza, V. M. (2017). Insights into the causal relationship between slow slip and tectonic  
764 tremor in Guerrero, Mexico. *Journal of Geophysical Research: Solid Earth*, 122(8), 6642-6656.  
765 <https://doi.org/10.1002/2017JB014037>
- 766 Yabe, S., Tanaka, Y., Houston, H., & Ide, S. (2015). Tidal sensitivity of tectonic tremors in Nankai and Cascadia  
767 subduction zones. *Journal of Geophysical Research: Solid Earth*, 120(11), 7587-7605.  
768 <https://doi.org/10.1002/2015JB012250>

769 Yamashita, T., & Tsutsumi, A. (2018). *Involvement of fluids in earthquake ruptures*. Tokyo, Japan: Springer.

770 <https://doi.org/10.1007/978-4-431-56562-8>